# Nuclear export governs TDP-43 phase transitions and cytoplasmic aggregation

Natalie Chin [1#], Qi Zhang [2#], Jizhong Zou [3], Ken Chih-Chien Cheng [4], Wei Zheng [2], Yihong Ye [1]

[1] Laboratory of Molecular Biology, National Institute of Diabetes, Digestive, and Kidney Diseases, National Institutes of Health, Bethesda, MD, 20892, USA

[2] Therapeutic Development Branch, National Center for Advancing Translational Sciences, National Institutes of Health, Bethesda, MD, 20892, USA

[3] iPSC Core, National Heart, Lung, and Blood Institute, National Institutes of Health, Bethesda, MD, 20892, USA

[4] Functional Genomics Laboratory, National Center for Advancing Translational Sciences, National Institutes of Health, Bethesda, MD, 20892, USA

Correspondence: yihongy@mail.nih.gov (Y.Y.)

# Equal contribution

**Keywords**: TDP-43, anisosome, protein aggregation, nuclear transport, XPO1, liquid-liquid phase separation/LLPS.

**RNA-binding protein TAR DNA-binding protein 43 (TDP-43) can form liquid-like, nuclear assemblies whose phase transitions are linked to protein aggregation and neurodegeneration. The mechanisms that determine whether these assemblies remain dynamic or convert into solid states are poorly defined. Here we combined chemical and genome-wide genetic screenings to identify cellular processes influencing the phase behavior of an RNA-binding defective TDP-43 mutant associated with amyotrophic lateral sclerosis (ALS) and frontotemporal dementia (FTD). While the screens identified multiple cellular processes—including RNA splicing, translation, and proteostasis—as modulators of TDP-43 phase states, our analyses underscore nuclear transport as a critical determinant of liquid-to-solid transitions. Inhibition of nuclear export prevents cytoplasmic accumulation of immobile TDP-43 assemblies, whereas enhanced export promotes irreversible, solid TDP-43 structures. We validated this mechanism in a brain organoid model of ALS, showing nuclear retention limits pathogenic aggregation and its associated defects. These findings establish nuclear export as a key regulator of TDP-43 phase transitions and define a mechanistic link between altered phase dynamics and neurodegeneration.**

The RNA-binding protein TAR DNA-binding protein 43 (TDP-43), encoded by the *TARDBP* gene, plays a central role in RNA transport, splicing and metabolism (Guo and Shorter, 2017; Suk and Rousseaux, 2020), and is the major pathological component of cytoplasmic inclusions in amyotrophic lateral sclerosis (ALS) and frontotemporal dementia (FTD) patients (Kellett et al., 2025; Neumann et al., 2006; Rummens and Da Cruz, 2025). TDP-43 contains two RNA-recognition motifs (RRMs), a bipartite nuclear-localization sequence, and a glycine-rich C-terminal low-complexity domain (LCD) that is intrinsically prone to aggregation (Tziortzouda et al., 2021). Under physiological conditions, TDP-43 binds RNAs in the nucleus, participating in multiple RNA-metabolic processes. In contrast, disease-causing mutations trigger its mis-localization to the cytoplasm, forming detergent-resistant inclusions. TDP-43-positive protein aggregates were present in ~97% of ALS and ~45% of FTD cases, as well as in a subset of Alzheimer's disease patients. These diseases are now collectively termed TDP-43 proteinopathies (Brettschneider et al., 2014; Neumann et al., 2006). Both loss of nuclear function and gain of cytoplasmic toxicity have been implicated in neurodegeneration (Suk and Rousseaux, 2020; Tziortzouda et al., 2021), underscoring the importance of nucleocytoplasmic transport in regulating TDP-43 patho-physiological functions.

Like many RNA-binding proteins (RBPs), TDP-43 undergoes liquid-liquid phase separation to form membraneless biomolecular condensates (Conicella et al., 2016; Shorter, 2019; Tziortzouda et al., 2021). Under conditions of cellular stress or in the presence of RNA-binding defective mutations, these condensates can transition from dynamic liquid droplets to more rigid gel-like or solid assemblies (Conicella et al., 2016; Gasset-Rosa et al., 2019; Lang et al., 2024). To date, more than 70 disease-linked mutations in *TARDBP* have been identified in ALS or FTD, many within the LCD, while others clustering near or in the RRMs disrupt RNA binding (Tziortzouda et al., 2021). Defects in RNA binding appears to be a major governor of TDP-43 phase behavior (Babinchak et al., 2019; Mann et al., 2019). Additionally, disease-associated mutations alter TDP-43's regulatory functions in RNA metabolism, causing widespread cryptic exon inclusion (Ling et al., 2015; Ma et al., 2022; Mehta et al., 2023; Seddighi et al., 2024; Zhang et al., 2025b), alternative polyadenylation and other RNA maturation defects that collectively contribute to neurotoxicity (Zeng et al., 2025).

A major advance in the field of TDP-43 phase regulation is the recent report of a unique form of TDP-43 demixing, forming "anisosomes" that contain an anisotropic spherical shell of an RNA-binding-defective TDP-43 mutant and a central liquid core formed by the HSP70 chaperone (Yu et al., 2021). These structures, observed mostly in the nucleus, were postulated to be an intermediate en route to pathological aggregation when cellular proteostasis or nucleocytoplasmic transport is compromised. Additionally, in vitro studies with purified TDP-43 and selected small molecules have begun to elucidate

the molecular basis of TDP-43 self-association (Maurel et al., 2025; Rubien et al., 2022), offering insights into its phase behavior and aggregation mechanisms.

Despite these advances, the cellular pathways modulating TDP-43 phase behavior (droplet formation, anisosomal shell–core architecture, conversion to gel/solid structures) and its link to disease-associated aggregation remain poorly defined. Here, we address this knowledge gap by combining a chemical-genetic screen approach with a genome-wide siRNA screen to identify molecular determinants that modulate the phase behavior of an RNA-binding defective TDP-43 mutant. Our study reveals critical contributions of RNA splicing, protein translation, and the HSP90/ubiquitin–proteasome proteostasis network to TDP-43 phase transitions. Importantly, our work demonstrates how nuclear export can influence the transition of TDP-43 from a nuclear liquid-demixed form to a cytoplasmic immobile structure. We validated the impact of nuclear export inhibition on phosphorylated-TDP-43 cytoplasmic accumulation using an iPSC-derived 3-D organoid model bearing an ALS-associated mutation (Zhang et al., 2025b). Collectively, these findings establish a mechanistic framework linking altered phase dynamics and TDP-43 aggregation to nuclear transport defects, a process known to modulate neurodegeneration in ALS and FTD.

## Results

### A chemical genetic screen identified modulators of TDP-43 phase behavior

To identify cellular pathways modulating TDP-43 phase behavior, we conducted a chemical genetic screen using a small molecule library targeting diverse known cellular pathways and processes. We employed a previously established DLD1 cell model stably expressing an RNA-binding defective TDP-43 mutant (2KQ) tagged with the green fluorescence protein Clover because TDP-43 2KQ undergoes rapid demixing in the nucleus upon expression induction (Yu et al., 2021). We seeded cells in 384-well plates and induced the expression of TDP-43 2KQ with doxycycline for 24 hours. We then treated these cells with a LOPAC library containing 1280 drugs for 24 hours (Figure 1A). This approach could avoid false positive drugs that affect the induction of TDP-43 2KQ.

High content imaging combined with algorithm-based image analyses (see methods) detected ~20 spherical anisosomes per cell in controls and most treated cells. However, in cells treated with a subset of the drugs, the number of anisosomes was noticeably reduced (Supplemental Table 1). Importantly, cells treated with Bortezomib, a potent proteasome inhibitor, had fewer but enlarged TDP-43 positive punctae with irregular shapes (Figure 1B), similar to cells treated with another proteasome inhibitor reported previously (van Eersel et al., 2011; Yu et al., 2021). This result validated our screening design.

To further confirm the identified hits, we performed a titration experiment, which showed that these inhibitors dose-dependently reduced the number of anisosomes with $IC_{50}$ ranging from sub-

micromolar to micromolar (Figure 1B, Supplemental Table 1). Interestingly, the screen identified cytoplasmic signaling kinases including PAK4, BTK, and GSK-3β as well as the receptor tyrosine kinase PDGFRβ as modulators of TDP-43 phase behavior (Figure 1B, Supplemental Table 1). PAK4 and GSK-3β are known regulators of the YAP signaling pathway (Jin et al., 2025; Mo et al., 2024), and YAP was recently identified as a TDP-43-interacting protein that influences its phase dynamics (Zhang et al., 2025a). These connections provide additional physiological support for the relevance of the modulators uncovered in our screen. Our screen also linked TDP-43 2KQ demixing to protein translation because cycloheximide, a ribosome elongation inhibitor could modulate TDP-43 phase dynamics (see below).

**Live cell imaging revealed two distinct types of TDP-43 phase modulators**

We next used confocal microscopy to further characterize the impact of a subset of the identified inhibitors on anisosome dynamics. We chose Tripterin (a drug targeting the heat shock protein HSP90), CP-673451 (a PDGFRβ inhibitor), two deubiquitinase inhibitors VLX-1570 and Spautin-1, and the Exportin-1 inhibitor KPT-276 because previous reports have linked the targets of these compounds to TDP-43 proteinopathies (Archbold et al., 2018; Farrawell et al., 2020; Furukawa et al., 2015; Garcia-Toscano et al., 2024). We first induced anisosome formation for 24 hours and then treated cells with the inhibitors. Compared to DMSO-treated controls, cells treated with Spautin-1 had fewer and smaller anisosomes. KPT-276 treatment also reduced anisosome number, albeit to a lesser extent (Figure 2A, top panels). In contrast, cells treated with CP-673451, Tripterin, or Bortezomib had fewer but larger TDP-43 punctae. Since Tripterin was also reported as a 20S proteasome inhibitor, we confirmed the role of HSP90 in this process by treating cells with the well-established HSP90 inhibitor Geldanamycin, which caused similar phenotypes as Tripterin (Supplemental Figure 1A). These results suggest that TDP-43 phase dynamics are modulated by the cellular folding capacity, the ubiquitin proteasome system, and nucleocytoplasmic transport.

To further dissect the effects of these inhibitors on TDP-43 phase separation, we combined drug treatment with live cell fluorescence imaging, using Fluorescence Recovery After Photobleaching (FRAP) or reversed FRAP to define the dynamics of TDP-43 2KQ. In FRAP, when the green fluorescence of anisosomes was bleached by a laser in untreated cells, it rapidly recovered due to the recruitment of TDP-43 2KQ from the nucleoplasm (Figure 2B, top panels, Figure 2C, D). Conversely, in reversed FRAP, bleaching TDP-43 2KQ surrounding an anisosome and then imaging the anisosome over time revealed a gradual decline in fluorescence intensity within the unbleached anisosome, while the surrounding bleached anisosomes regained some fluorescence (Figure 2E, top panel). This result suggests that TDP-43 2KQ in anisosomes could also be released into the nucleoplasm. Interestingly, in cells treated with Spautin-1 or KPT-276, anisosome-associated TDP-43 2KQ could freely exchange with the nucleoplasmic

pool (Figure 2B, D). However, in cells treated with Bortezomib, Tripterin or Geldanamycin, the enlarged TDP-43 puncta appeared static; TDP-43 2KQ fluorescence within anisosomes failed to recover after photobleaching (Figure 2B, C, Supplemental Figure 1B), nor did it decrease over time when surrounding TDP-43 2KQ was bleached (Figure 2E-G). Collectively, these results suggest that these inhibitors affect anisosomes via two distinct mechanisms: one maintains TDP-43 in a demixed liquid state, while the other converts it to a gel-like, solid state.

**A genome-wide siRNA screen identified genetic modulators of TDP-43 phase separation**

To further decipher the molecular determinants of TDP-43 phase separation, we conducted an unbiased genome-wide siRNA knockdown (KD) screen (Figure 3A). To this end, we transfected a siRNA library targeting 21,404 human genes each with three siRNAs into DLD1 cells stably expressing Clover-tagged TDP-43 2KQ. After gene KD, anisosomes were induced for 24 hours. High content imaging and automated analysis identified 1,533 candidates whose KD reduced the anisosome number per cell (Z-score > 2) (Supplementary Table S2). Based on a STRING gene network analysis, we selected 211 networked genes with top Z-scores and re-screened each of them with three additional siRNAs. This confirmed the involvement of 110 genes in TDP-43 anisosome regulation (Figure 3A, Supplementary Table S3). GO pathway analyses categorized identified genes into several major pathways including RNA splicing, protein translation, proteasomal degradation, and nuclear transport (Figure 3B). The identification of large number of ribosomal proteins and proteasome subunits is consistent with our chemical genetic screen, which showed that translation and proteasome inhibitors modulate anisosomes (Supplemental Table 1). Interestingly, GO analyses using ‘molecular function’ further linked many identified genes to neurodegenerative diseases, particularly ALS (Figure 3C, D).

**Anisosome dynamics is modulated by RNA splicing and protein translation**

Given the well-established function of TDP-43 in RNA binding and processing, we investigated the role of RNA splicing in anisosome regulation. To this end, we first incubated Clover-tagged TDP-43 2KQ cells with doxycycline to induce anisosomes and then treated cells with the potent RNA splicing inhibitor Pladienolide-B (PlaB). Confocal microscopy confirmed that RNA splicing inhibition resulted in fewer but larger TDP-43-positive puncta in a dose dependent manner (Figure 4A, B, Supplemental Figure 2A). Despite the size difference, anisosomes in drug-treated cells were morphologically indistinguishable from controls. FRAP experiments further showed that TDP-43 within PlaB-treated condensates remained highly mobile, although the fluorescence recovery rate was slightly reduced compared to controls (Figure 4C, D). Time-lapse live cell imaging frequently detected fusion of TDP-43 puncta after PlaB treatment

(Figure 4E, Movie S1). Together, these results suggest that disrupting RNA splicing stabilizes TDP-43 in demixed liquid state, resulting in larger condensates.

Next, we explored the effect of translation inhibition on anisosome dynamics using Cycloheximide (CHX) and Anisomycin (ANS). Confocal imaging showed that after anisosome induction, translational shutdown by CHX or ANS did not significantly reduce TDP-43 expression, suggesting a long half-life. Similar to PlaB-treated cells, CHX- and ANS-treated cells contained fewer, enlarged anisosomes (Figure 4F-H, Supplemental Figure S2B). FRAP analysis revealed that TDP-43 dynamics within anisosomes were similar between ANS-treated and control cells (Figure 4I, J). These results suggest that translation inhibition also stabilizes TDP-43 in liquid condensates.

**Nuclear export regulates TDP-43 liquid-to-solid phase transition**

Our screen also identified several nuclear transport regulators (e.g., Exportin-1/XPO1, Exportin-2/CSE1L) and nuclear pore components as anisosome regulators (Figure 3B). We focused on XPO1 because our chemical genetic screen identified two XPO1 inhibitors, KPT-276 and Verdinexor as potent anisosome modulators (Figure 1B).

To explore the role of XPO1 in TDP-43 anisosome regulation, we induced anisosome formation in Clover-TDP-43 2KQ cells and treated them with Leptomycin B (LMB), a potent XPO1 inhibitor. LMB treatment resulted in a time- and dose-dependent reduction in anisosome number, while increasing their sizes (Figure 5A-C). The enlarged TDP-43 puncta showed the typical hollowed anisosome ring structure (Figure 5D), indicating that TDP-43 remained in the liquid state. Indeed, FRAP experiments demonstrated that LMB treatment did not significantly affect the fluorescence recovery rate of TDP-43 within bleached anisosomes (Figure 5D, E). Time-lapse confocal imaging showed that shortly after LMB treatment, preformed anisosomes began to fuse with each other (Figure 5F, Movie S2). Thus, XPO1 inhibition stabilizes TDP-43 in a liquid phase.

To corroborate the inhibitor study, we overexpressed mCherry-tagged XPO1. Surprisingly, we observed fewer and enlarged TDP-43 positive puncta in mCherry-XPO1-expressing cells (Figure 5G, panels 1, 2). At first glance, this phenotype resembled that of XPO1-inhibited cells. However, careful examination revealed several distinct features. First, despite the size increase, we did not observe the typical hollowed anisosome ring structure. Secondly, while anisosomes in mCherry-XPO1 negative cells were almost exclusively nuclear, ~30% of mCherry-XPO1-expressing cells contained cytoplasm-localized TDP-43 puncta (Figure 5G, panels 1, 2, 3, Figure 5H). Thirdly, FRAP experiments demonstrated that Clover-TDP-43 fluorescence did not recover after photobleaching, suggesting that TDP-43 was in a gel-like state transitioning to aggregates (Figure 5I). Notably, mCherry-XPO1 could be detected within TDP-43 puncta in some cells (Figure 5G, panels 3-6). These findings are consistent with a

previous report (Archbold et al., 2018), demonstrating that XPO1 promotes TDP-43 nuclear egression and cytoplasmic aggregate formation. Immunostaining of endogenous XPO1 in anisosome-induced cells further confirmed this conclusion. Although antibodies could not penetrate anisosomes (Yu et al., 2021), anisosome induction depleted XPO1 from the nucleoplasm, presumably due to its sequestration into anisosomes (Figure 5J, K). Since XPO1 does not bind TDP-43 directly (Pinarbasi et al., 2018), additional factors likely facilitate XPO1-mediated TDP-43 nuclear egression under this condition. Collectively, these results suggest that the stability and dynamics of anisosomes are modulated by XPO1: reduced XPO1 activity stabilizes the liquid state and favors large TDP-43 condensates, whereas increasing XPO1 activity promotes its transition to a gel-like structure and cytoplasmic redistribution (Figure 5L). This conclusion underscores a critical regulatory link between XPO1-dependent nuclear egression and the TDP-43 liquid-to-solid phase transition.

**XPO1 inhibition mitigates TDP-43 hyperphosphorylation and modest rescues neuronal defects in an anisosome-bearing organoid model**

Since increased XPO1 activity is associated with more cytoplasmic, gel-like TDP-43, we tested whether reducing XPO1 activity could mitigate TDP-43 cytosolic aggregation using a recently established anisosome-bearing organoid model of TDP-43 proteinopathies. This model is derived from an induced pluripotent stem cell (iPSC) line carrying the ALS-associated mutation (K181E) (Zhang et al., 2025b), which like 2KQ disrupts the RNA binding activity of TDP-43 (Chen et al., 2019). Additionally, the K181E mutant accumulates in a liquid-condensed phase in association with HSP70, and like anisosomes, these condensates can convert to solid aggregates during cellular stress or HSP70 depletion (Gu et al., 2021).

We treated homozygous K181E organoids or wild-type (WT) controls with KPT-276 at a low dose (20 nM) for 35 days, starting on day 87 based on pilot data indicating good tolerance with prolonged treatment. Since hyperphosphorylated TDP-43 (p-TDP-43) is a major aggregate component, we stained organoids with antibodies against p-TDP-43 and total TDP-43. Confocal imaging revealed that WT and K181E organoids had similar amounts of total TDP-43, but p-TDP-43 was only significantly present in mutant organoids (Figure 6A), as reported previously (Zhang et al., 2025b). KPT-276 did not alter the total TDP-43 levels in either genotype (Figure 6A) but significantly reduced the cytosolic p-TDP-43 positive puncta in K181E organoids (Figure 6A, B).

To assess whether KPT-276 treatment also rescued the neuronal defects in TDP-43 K181E organoids, we performed bulk RNAseq using KPT-276-treated K181E and WT organoids. A comparison of treated mutant organoids to WT or untreated K181E organoids showed that KPT-276 reversed expression defects in 58 downregulated (2.90%) and 45 (1.99 %) upregulated genes (Supplemental Figure

3, Supplemental Table S4). GO pathway analysis of genes rescued from downregulation by KPT-276 highlighted neuronal pathways including neuron differentiation and brain development; for genes upregulated in K181E organoids, rescued genes are linked to G-protein coupled neurotransmitter receptor activities at the plasma membranes (Figure 6C, Supplementary Table S4). Together, these results demonstrate that XPO1 inhibition by KPT-276 modestly restores gene transcription defects in a subset of neuronal pathways in K181E mutant organoids, while robustly mitigating FTD-associated p-TDP-43 accumulation. Thus, reducing TDP-43 cytoplasmic aggregation alone may offers only limited benefit in disease treatment.

**Discussion**

ALS- and FTD-associated TDP-43 mutants defective in RNA binding are known to undergo self-association through their intrinsically disordered regions and RNA-binding domains, generating demixed liquid, gel, and aggregated states that remain in dynamic exchange. This protein phase behavior is shared by many RNA binding proteins and is increasingly recognized as a contributor to protein aggregation in neurodegenerative diseases (Shorter, 2019). Intriguingly, TDP-43 phase separation forms unique layered nuclear structures, with an HSP70-filled central core surrounded by a protein shell made of TDP-43. Although it is unclear how these structures are nucleated in the cell, our observations suggest that, once formed, they can grow by recruiting additional TDP-43 from the surrounding environment. Small anisosomes may also fuse with one another, although such fusion events become infrequent and difficult to detect after anisosomes reach a steady state,

Our study supports the notion that TDP-43, at high concentrations, can transition from a demixing-prone, liquid state into a gel-like state en route to forming amorphous aggregates (Babinchak et al., 2019; Carey and Guo, 2022). We found that inhibition of RNA splicing, protein translation, or nuclear export favors the liquid state of TDP-43, while proteasome and HSP90 inhibition or enhancing XPO-1-mediated nuclear egression promotes the conversion of anisosomes to a gel-like state.

Because the TDP-43 2KQ mutant lacks RNA binding activity, the effects of splicing inhibition are likely mediated by other RNA-binding factors involved in splicing regulation. TDP-43 is known to interact with many splicing factors including members of the hnRNP family like hnRNP A1/A2 and PSF (Freibaum et al., 2010); Inhibition of RNA splicing may alter TDP-43's interactions with these factors, trapping it in certain complexes that favor its retention in the liquid state. Alternatively, splicing inhibition may change the overall nuclear environment, allowing large anisosomes to fuse with each other as observed in our study. This could explain why PlaB treatment reduces the number of TDP-43 anisosomes while maintaining their dynamic liquid property. Likewise, inhibition of nuclear export may influence anisosome dynamics by reshaping the nuclear environment, lowing the barrier to anisosome fusion.

Future studies are required to elucidate the precise mechanisms by which these pathways regulate anisosome dynamics.

Our validation of proteasome inhibition as a driver of TDP-43 droplet enlargement and hardening reinforces the idea that impaired protein clearance promotes the transition from liquid condensates to gel-like or solid aggregates. This is consistent with previous studies in ALS models, which showed that proteasome stress accelerates TDP-43 aggregation and toxicity (van Eersel et al., 2011). In contrast, inhibition of deubiquitinases reduced the number of TDP-43 anisosomes, probably by promoting the proteasome-mediated clearance of TDP-43. The role of HSP90 in this process may be linked to TDP-43 folding stability, as HSP90 can bind TDP-43 to prevent promiscuous interactions (Lin et al., 2021). Collectively, these observations suggest that TDP-43 condensates are maintained by a delicate balance between formation and clearance, modulated by proteolytic and chaperone activities.

While out chemical and genetic screens have identified multiple pathways influencing TDP-43 phase states, a particularly compelling aspect of our study is the discovery that the nuclear export receptor XPO1 governs TDP-43 liquid-to-solid transitions and subcellular localization. Pharmacological inhibition of XPO1 mitigates cytoplasmic p-TDP-43 accumulation, whereas XPO1 overexpression promotes the cytoplasmic accumulation of TDP-43-containing puncta. However, XPO1 may modulate TDP-43 nuclear egression indirectly, as suggested previously (Duan et al., 2022; Pinarbasi et al., 2018). While previous studies have not detected strong interactions between XPO-1 and TDP-43 (Pinarbasi et al., 2018), a weak or indirect interaction between XPO-1 and TDP-43 may still exist, especially when TDP-43 undergoes demixing. This model would explain why anisosome induction depletes endogenous XPO-1 from the nucleoplasm. Our findings also hint at a potential feedback mechanism in which TDP-43 demixing perturbs nuclear export, analogous to how cytoplasmic TDP-43 aggregates disrupt nuclear import. Given that ALS is characterized by cytoplasmic TDP-43 mis-localization and hyperphosphorylation, the XPO-1-dependent nuclear export pathway may constitute a key molecular switch linking physiological phase behavior to pathological aggregation.

Notably, in 3-D brain organoids bearing the K181E mutation, inhibition of nuclear export by KPT-276 only modestly rescues the transcriptional defects in homozygous TDP-43 K181E organoids despite an almost complete ablation of cytoplasmic phospho-TDP-43. This observation suggests that cytoplasmic TDP-43 aggregation is only a modest contributor to TDP-43 proteinopathies that lead to neurodegeneration. Major defects may still be attributed to deregulated RNA processing due to altered RNA binding (Hergesheimer et al., 2019; Joseph et al., 2025; Mehta et al., 2023; Zhang et al., 2025b). Thus, effective therapy likely requires both inhibition of cytoplasmic TDP-43 aggregation and restoration of normal RNA processing and nuclear transport. Together, our results support a model in which multiple cellular pathways including proteostasis, RNA metabolism, translation, and nuclear export—

cooperatively determine the phase behavior of TDP-43. These findings have deepened our understanding of how physiological phase separation can evolve into pathogenic aggregation through cumulative failures of cellular quality control and nuclear export systems.

## Methods

### RNAi-based genetic screen for anisosome regulators

Genome-wide RNA interference (RNAi) screen was performed using DLD1 cells stably expressing Clover-tagged TDP-43 2KQ. Cells were transfected with siRNAs targeting 21,404 genes for 72 hours, followed by induction of anisosome formation with doxycycline (0.5 µg/mL) for 24 h. Specifically, the screen was carried out in 384-well format with 3 individual siRNAs for each gene. To prepare siRNA transfection, control siRNA (40 nmol) was mixed with 2 mL water to create a 50X (20 µM) stock and siRNA-death (20 nmol) was mixed with 1 mL of water for the same concentration. Dilute siRNA stocks to a 400 nM working concentration in water. For each well, mix 0.1 µL transfection reagent in 20 µL of cell culture medium without FBS or P/S. Add 2 µL of siRNA solution to each well and incubate with RNAiMAX for 30 minutes at room temperature. While incubating RNAiMAX, prepare trypsinized cells by ensuring thorough separation and accurate cell counting. Add 20 µL of cell suspension at a density of $0.43 \times 10^5$ cells/mL (850 cells/well) in medium containing 20% FBS and 2 x P/S to achieve a final volume of 40 µL per well. Incubate cells for 3 days before addition of 10 µL 10 x doxycycline solution to each well (final volume 50 µL) for anisosome induction. 24 h later, high-throughput (HT) imaging and automated phenotypic screening were conducted to identify genes that modulated anisosome formation.

Fluorescence imaging was conducted using an Opera Phenix High-Content Screening System (PerkinElmer). Whole-well images were acquired in confocal mode using a 20X water objective lens after anisosome induction for 24 h. Images were reconstructed and analyzed using the PerkinElmer Columbus server (v2.9.1). Nuclei were segmented based on Hoechst33342 staining, and anisosomes were detected via YFP signals within the nuclear region. The mean anisosome count per nucleus was calculated to assess changes in anisosome levels, while toxicity was evaluated by counting the total number of nuclei. Data were normalized to the siRNA-Neg control for each plate, and Z-scores were calculated to identify significant hits. Identified 1,533 genes whose knockdown significantly reduced the number of anisosomes per cell (Z-score > 2) were subjected to protein network analysis by STRING to identify candidate anisosome regulatory genes that were subject to a second-round screen.

### A chemical genetic screen for anisosome regulators

We also performed a chemical genetic screen using LOPAC$^{R1280}$ (Sigma) compound library on DLD1 cells expressing Clover-tagged TDP-43-2KQ. Briefly, cells were induced with doxycycline for 24 h to

promote anisosome formation, followed by treatment with individual compounds for an additional 24 hours. High-throughput (HT) imaging and automated phenotypic screening were conducted to identify compounds that modulated anisosome formation.

**Visualization and analysis of anisosome dynamics**

To examine the impact of drug treatment on anisosome size, cells were induced to form anisosome for 24 h and then treated by different inhibitors as follows: cycloheximide (CHX, 20 µg/mL), anisomycin (ANS, 200 nM) for 16 hours. For splicing inhibition, cells were exposed to Pladienolide-B (PlaB) at concentrations of 5 or 20 nM, or DMSO (control) for 16 hours before imaging. Cells were fixed with 4% paraformaldehyde in Phosphate Buffer Saline (PBS). Randomly selected fields were used to quantify the number of anisosomes per cell with at least two biological repeats.

To image anisosome fusion, live cell imaging was performed by treating cells with Leptomycin B (200 nM) or PlaB (20 nM) for 5 hours and then imaged by confocal 3-D sectioning for 30 minutes to capture anisosome fusion events. For Fluorescence Recovery After Photobleaching (FRAP), cells were treated with DMSO, Leptomycin B, Geldanamycin or PlaB as indicated in figure legends. Either part of an anisosome or entire anisosome was photobleached and imaged. TDP-43 fluorescence recovery after photobleaching was quantified by ImageJ and calculated to assess anisosome dynamics. At least 10 anisosomes for each condition were bleached and analyzed.

To evaluate the time course of Leptomycin B (LMB)-induced anisosome changes, DLD1 TDP-43 2KQ-Clover cells were seeded and induced with 0.5 µg/mL doxycycline for 24 hours. Cells were treated with 10 µM LMB and fixed at 0-, 8-, and 16-hours post-treatment. Fixed cells were stained with Hoechst to visualize nuclei. 10-20 confocal 3-D sections were obtained for each randomly selected field. Images were converted to maximum projected view by ImageJ before anisosome counting and intensity measurement. The density plot of anisosome counts per cell was generated using R, illustrating dose-dependent effects of leptomycin on anisosome formation.

To test the effect of XPO1 overexpression on TDP-43 phase regulation, DLD1 TDP-43 2KQ-Clover cells were co-transfected with mCherry-tagged XPO1 (mCh-XPO1) for 24 h before doxycycline was added at 0.5 µg/mL to induce anisosome formation for 24 h before confocal imaging.

To study the relationship between anisosome induction and endogenous XPO1 localization, cells were seeded, induced with 0.5 µM doxycycline for 48 hours, and fixed with paraformaldehyde in PBS. Immunostaining was performed using an XPO1 antibody (Cell Signaling, 46249S, 1:125) and Hoechst nuclear stain. Fluorescence intensity of XPO1 in both induced and uninduced cells was measured by ImageJ.

**Experiments with organoids**

Stem cell gene editing of the patient K181E mutation in iPSC cells was reported previously (Zhang et al., 2025b). Differentiation of iPSCs into forebrain neurons was performed following a previously published protocol (Fernandopulle et al., 2018). Briefly, the procedure used an induction medium (IM-N2) and a neuronal culture medium (CM). IM-N2 was prepared with Knockout DMEM/F12, N2 supplement, NEAA, Gluta-MAX, Chroman I, and doxycycline. On Day 0, iPSCs were observed for confluency, dissociated with Accutase, centrifuged, and resuspended in IM-N2 with Chroman I, and then seeded into Matrigel-coated plates. Over the next four days, cells were monitored microscopically for neurite extensions while media containing doxycycline is refreshed daily. By Day 4, cells exhibit neurite growth and are ready for replating onto poly-L-ornithine (PLO)-coated dishes, prepared in advance by coating with PLO solution, incubating, washing, and drying. Replated cells were cultured in CM comprising BrainPhys medium, B27+ supplement, neurotrophic factors (GDNF, BDNF, NT-3), laminin, and doxycycline, to promote neuronal maturation.

3-D culture and organoid growth were performed as previously described (Nguyen, 2022). In brief, iPSCs grown on Matrigel were dissociated into single cell suspension by Versene solution (ThermoFisher) and seeded into a 12-well Aggrewell plate (Stemcell Technologies) at 4,000 cells/ well. Next day, spheroids were transferred to an ultralow attachment plate (Corning) containing phase I medium: DMEM/F12, 20% Gibco KnockOut Serum Replacement, 1X Glutamax, 1X MEM Nonessential Amino Acid, 55 µM β-Mercaptoethanol, 1X Pen/Strep, 2 µM Dorsomorphine, 2 µM A83-01. After 5 days, medium was switched to phase II medium: DMEM/F12, 1X N-2 Supplement, 1X Glutamax, 1X MEM Nonessential Amino Acid solution, 1X Pen/Strep, 4 ng/mL WNT3a, 1 µM CHIR-99021, 1 µM SB-431542. On day 7, spheroids were embedded into Matrigel and allowed to continue growing for 7 more days. On day 14, individual spheroids were manually freed from the Matrigel and transferred to a SpinOmega bioreactor spinning at 120 RMP with phase III media: DMEM/F12, 1X N-2 Supplement, 1X B-27 Supplement, 1X Glutamax, 1X MEM Nonessential Amino Acid, 55 µM 2-Mercaptoethanol, 1X Pen/Strep, 2.5 µg/mL insulin. 50 days later, the medium was switched to final differentiation medium: Neurobasal medium, 1X B-27 Supplement, 1X Glutamax, 55 µM 2-Mercaptoethanol, 1X Pen/Strep, 0.2 mM Ascorbic acid, 0.5 mM cAMP, 20 ng/mL brain-derived neurotrophic factor (BDNF), 20 ng/mL glial-derived neurotrophic factor (GDNF). 107-day-old organoids were dissociated into single cells using a 50:50 mixed of Accutase and 0.25% Trypsin with DNase I (1 mg/mL) and plated onto chambered glass slides pretreated with 1% Matrigel (Corning, Inc). Alternatively, organoids were fixed and sectioned for immunostaining (see below). For drug treatment, forebrain organoids (87 Day) were transferred to a 12-well plate on an orbital shaker (120 RPM) and treated with 20 nM KPT276 in final differentiation

medium. Medium was changed every other day (Dexoregen, Inc). The organoids were harvested and frozen after 35 days of treatment for sectioning or RNAseq analysis.

**Tissue preparation and immunostaining**

Organoids were fixed in 4% paraformaldehyde in PBS for 1 hour at room temperature, washed with PBS, and immersed in 15% sucrose/PBS solution overnight. Subsequently, organoids were embedded in O.C.T. compound (Sakura) in a plastic mold and frozen down in an ultralow freezer. Embedded organoids were sliced onto glass slides using a Cryostat (Leica). Slides were rinsed with PBS, permeabilized with 0.5% Triton-X/PBS solution for 1 hour at room temperature and blocked using 1% donkey serum in 0.1% Tween-20/PBS solution for 1 hour. Primary antibodies, chicken anti-TUJ1 (Abcam, Ab41489,1:1,000 dilution), rabbit anti-TDP-43 (10782-2-AP, 1/1000 dilution), mouse anti-phospho-TDP-43 (Cosmobio, CAC-TIP-PTD-M01A, 1/500 dilution), were added to the slides and the slides were incubated in a humidified chamber at 4 °C overnight. After several washes in 0.1% Tween-20/PBS solution, DAPI (Sigma) or secondary antibodies, donkey anti-rabbit, anti-mouse, and anti-chicken (Jackson ImmunoResearch), diluted 1:1,000 in blocking solution, were added to the slides. After 1 hour of incubation at room temperature, the slides were washed and mounted in antifade mounting solution (Fisher scientific).

**Image acquisition and processing**

Fluorescence confocal images were acquired using a Nikon CSU-W1 SoRa microscope equipped with temperature and $CO_2$ control enclosures and a 60x TIRF lens. Image reconstructions and analyses, including 3-D and time lapse visualizations, were performed using Imaris software or Image J. Fluorescence intensity was quantified using the open-source Fiji/Image J software. Images of randomly selected fields were split into individual channels. A consistent threshold method was applied to individual channel. The particle analysis function was used to automatically identify all anisosomes or other fluorescence structures for size and intensity measurement. Statistical analyses were conducted using Excel (for Student’s t-test) or GraphPad Prism versions 8.0 and 9.0. P-values were calculated using Student's t-test in Excel or one-way ANOVA in GraphPad Prism. Curve fitting, including linear and nonlinear models, as well as $IC_{50}$ calculations, were also performed using GraphPad Prism versions 8.0 and 9.0.

**Bulk RNA-seq library preparation and data analysis**

800 ng of total RNA samples to generate the library with the NEBNext rRNA Depletion Kit v2 (Human/ mouse/rat) (NEB #E7405), NEBNext Ultra II Directional RNA Library Prep Kit for Illumina (NEB

#E7760) and NEBNext® Multiplex Oligos for Illumina® (96 Unique Dual Index Primer Pairs, NEB, E6440) as described in the manufacturer's manual. Sequencing carried out in the Illumina NextSeq2000 instrument with 101x101 pair end configuration by NCI genomic core.

Adapters were trimmed using Cutadapt (v4.7), and reads were aligned to the GRCh38 genome build with STAR (v2.7.11b) using gene annotations from GENCODE v42. Gene expression was quantified with HTSeq (v2.0.7) (Putri et al., 2022), utilizing the same gene annotations. For differential gene expression analysis, all samples were processed uniformly following the standard DESeq2 (Love et al., 2014) workflow. Differential expression was defined based on an adjusted P-value threshold of <0.05 and |log2 fold change ($\log_2$FC) > 1. To identify gene expression rescued by exportin-1 inhibitor treatment, the fold change of expression level should be less than without inhibitor treatment, with P-value < 0.05.

**Statistic and reproducibility**

All statistical analyses were conducted with GraphPad Prism v10 or Excel. Statistical methods and the number of cells or brain organoid samples (N) are indicated in figure legends or shown in figures as individual data point. Biological repeats (n) are specified in figure legends. No biological repeat was excluded from the analyses. All experiments were repeated at least twice with individual data point labeled in figures unless specified. For imaging analyses, cells in randomly selected fields were analyzed. The researchers were not blinded. The iPSC cell line was derived from a ADRDs genetic risk-free clone, which was initially obtained from a male. Figures were prepared using ImageJ 1.54f, Imaris 9.9.0, Adobe Photoshop v25.12.1, and Adobe Illustrator 28.7.4.

**Data and code availability**

Raw and processed bulk RNA-seq data can be accessed from Sequence Read Archive (SRA), NCBI with Bioproject ID: PRJNA1195353, http://www.ncbi.nlm.nih.gov/bioproject/1195353.

**Author contributions**

YY conceived and designed the study. YY, KC and WZ supervised the study. QZ and KC conducted the chemical and siRNA screens. NC performed post-screen validation and characterization of anisosomes under different conditions. J Z constructed the iPSC knock-in lines and QZ conducted the organoid study. QZ, NC and YY analyzed the data. YY wrote the manuscript. All authors read, edited, and approved the manuscript.

**Corresponding authors**

Correspondence to Yihong Ye.

**Funding**

This work is supported by the Intramural Research Programs of NCATS (WZ & KC) and NIDDK (YY) at NIH.

**Declaration of Interests**

The authors declare no competing interests.

**Acknowledgements**

We thank the NIDDK Advanced Imaging Core with data acquisition. We thank D.W. Cleveland (UCSD) and H. Yu (Genentech) for providing the doxycycline-inducible DLD1 TDP-43 2KQ-Clover cell line and protocol. We thank K. Bharti and W. Li (NEI), Dr. T. Zhang (NIA) for critical reading of the manuscript. We also thank Drs. L. El Touny, D. Blivis, and T. Voss (NCATS) for their valuable support, as well as the NCATS Compound Management Group and the NCATS Automation Group for their contributions to the chemical and genetic screens.

**References**

Archbold, H.C., K.L. Jackson, A. Arora, K. Weskamp, E.M. Tank, X. Li, R. Miguez, R.D. Dayton, S. Tamir, R.L. Klein, and S.J. Barmada. 2018. TDP43 nuclear export and neurodegeneration in models of amyotrophic lateral sclerosis and frontotemporal dementia. *Sci Rep*. 8:4606.

Babinchak, W.M., R. Haider, B.K. Dumm, P. Sarkar, K. Surewicz, J.K. Choi, and W.K. Surewicz. 2019. The role of liquid-liquid phase separation in aggregation of the TDP-43 low-complexity domain. *J Biol Chem*. 294:6306-6317.

Brettschneider, J., K. Del Tredici, D.J. Irwin, M. Grossman, J.L. Robinson, J.B. Toledo, L. Fang, V.M. Van Deerlin, A.C. Ludolph, V.M. Lee, H. Braak, and J.Q. Trojanowski. 2014. Sequential distribution of pTDP-43 pathology in behavioral variant frontotemporal dementia (bvFTD). *Acta Neuropathol*. 127:423-439.

Carey, J.L., and L. Guo. 2022. Liquid-Liquid Phase Separation of TDP-43 and FUS in Physiology and Pathology of Neurodegenerative Diseases. *Front Mol Biosci*. 9:826719.

Chen, H.J., S.D. Topp, H.S. Hui, E. Zacco, M. Katarya, C. McLoughlin, A. King, B.N. Smith, C. Troakes, A. Pastore, and C.E. Shaw. 2019. RRM adjacent TARDBP mutations disrupt RNA binding and enhance TDP-43 proteinopathy. *Brain*. 142:3753-3770.

Conicella, A.E., G.H. Zerze, J. Mittal, and N.L. Fawzi. 2016. ALS Mutations Disrupt Phase Separation Mediated by alpha-Helical Structure in the TDP-43 Low-Complexity C-Terminal Domain. *Structure*. 24:1537-1549.

Duan, L., B.L. Zaepfel, V. Aksenova, M. Dasso, J.D. Rothstein, P. Kalab, and L.R. Hayes. 2022. Nuclear RNA binding regulates TDP-43 nuclear localization and passive nuclear export. *Cell Rep*. 40:111106.

Farrawell, N.E., L. McAlary, J.S. Lum, C.G. Chisholm, S.T. Warraich, I.P. Blair, K.L. Vine, D.N. Saunders, and J.J. Yerbury. 2020. Ubiquitin Homeostasis Is Disrupted in TDP-43 and FUS Cell Models of ALS. *iScience*. 23:101700.

Fernandopulle, M.S., R. Prestil, C. Grunseich, C. Wang, L. Gan, and M.E. Ward. 2018. Transcription Factor-Mediated Differentiation of Human iPSCs into Neurons. *Curr Protoc Cell Biol*. 79:e51.

Freibaum, B.D., R.K. Chitta, A.A. High, and J.P. Taylor. 2010. Global analysis of TDP-43 interacting proteins reveals strong association with RNA splicing and translation machinery. *J Proteome Res*. 9:1104-1120.

Furukawa, T., N. Matsui, K. Fujita, H. Nodera, F. Shimizu, K. Miyamoto, Y. Takahashi, T. Kanda, S. Kusunoki, Y. Izumi, and R. Kaji. 2015. CSF cytokine profile distinguishes multifocal motor neuropathy from progressive muscular atrophy. *Neurol Neuroimmunol Neuroinflamm*. 2:e138.

Garcia-Toscano, L., H.N. Currey, J.C. Hincks, J.G. Stair, N.J. Lehrbach, and N.F. Liachko. 2024. Decreased Hsp90 activity protects against TDP-43 neurotoxicity in a C. elegans model of amyotrophic lateral sclerosis. *PLoS Genet*. 20:e1011518.

Gasset-Rosa, F., S. Lu, H. Yu, C. Chen, Z. Melamed, L. Guo, J. Shorter, S. Da Cruz, and D.W. Cleveland. 2019. Cytoplasmic TDP-43 De-mixing Independent of Stress Granules Drives Inhibition of Nuclear Import, Loss of Nuclear TDP-43, and Cell Death. *Neuron*. 102:339-357 e337.

Gu, J., C. Wang, R. Hu, Y. Li, S. Zhang, Y. Sun, Q. Wang, D. Li, Y. Fang, and C. Liu. 2021. Hsp70 chaperones TDP-43 in dynamic, liquid-like phase and prevents it from amyloid aggregation. *Cell Res*. 31:1024-1027.

Guo, L., and J. Shorter. 2017. Biology and Pathobiology of TDP-43 and Emergent Therapeutic Strategies. *Cold Spring Harb Perspect Med*. 7.

Hergesheimer, R.C., A.A. Chami, D.R. de Assis, P. Vourc'h, C.R. Andres, P. Corcia, D. Lanznaster, and H. Blasco. 2019. The debated toxic role of aggregated TDP-43 in amyotrophic lateral sclerosis: a resolution in sight? *Brain*. 142:1176-1194.

Jin, Y., Y. Xue, J. Yao, C. Xu, and R. Yu. 2025. FBXO9 mediated the ubiquitination and degradation of YAP in a GSK-3beta-dependent manner. *J Biol Chem*. 301:110652.

Joseph, B.J., K.A. Marshall, P. Harley, J.R. Mann, F. Alessandrini, C.G. Vanoye, W. Chi, M. Prudencio, D. Simkin, T.T. Kao, R.R. Desai, M.J. Keuss, S. Barattucci, M. Zanovello, P.R. Mehta, J.M. DeKeyser, F. Limone, J. Lee, A.L. Brown, M.F. Leyton-Jaimes, L.A. Nash, I.G.S. Juan, E. Aronica, B.J. Wainger, M. Shah, A. Goswami, N.A. Shneider, D.W. Dickson, J. Burrone, C. Zhang, H. Wichterle, L. Petrucelli, J.K. Watts, A.L. George, Jr., P. Fratta, K. Eggan, and E. Kiskinis. 2025. TDP-43-dependent mis-splicing of KCNQ2 triggers intrinsic neuronal hyperexcitability in ALS/FTD. *Nat Neurosci*.

Kellett, E.A., A.T. Bademosi, and A.K. Walker. 2025. Molecular mechanisms and consequences of TDP-43 phosphorylation in neurodegeneration. *Mol Neurodegener*. 20:53.

Lang, R., R.E. Hodgson, and T.A. Shelkovnikova. 2024. TDP-43 in nuclear condensates: where, how, and why. *Biochem Soc Trans*. 52:1809-1825.

Lin, L.T., A. Razzaq, S.E. Di Gregorio, S. Hong, B. Charles, M.H. Lopes, F. Beraldo, V.F. Prado, M.A.M. Prado, and M.L. Duennwald. 2021. Hsp90 and its co-chaperone Sti1 control TDP-43 misfolding and toxicity. *FASEB J*. 35:e21594.

Ling, J.P., O. Pletnikova, J.C. Troncoso, and P.C. Wong. 2015. TDP-43 repression of nonconserved cryptic exons is compromised in ALS-FTD. *Science*. 349:650-655.

Love, M.I., W. Huber, and S. Anders. 2014. Moderated estimation of fold change and dispersion for RNA-seq data with DESeq2. *Genome Biol*. 15:550.

Ma, X.R., M. Prudencio, Y. Koike, S.C. Vatsavayai, G. Kim, F. Harbinski, A. Briner, C.M. Rodriguez, C. Guo, T. Akiyama, H.B. Schmidt, B.B. Cummings, D.W. Wyatt, K. Kurylo, G. Miller, S. Mekhoubad, N. Sallee, G. Mekonnen, L. Ganser, J.D. Rubien, K. Jansen-West, C.N. Cook, S. Pickles, B. Oskarsson, N.R. Graff-Radford, B.F. Boeve, D.S. Knopman, R.C. Petersen, D.W. Dickson, J. Shorter, S. Myong, E.M. Green, W.W.

Seeley, L. Petrucelli, and A.D. Gitler. 2022. TDP-43 represses cryptic exon inclusion in the FTD-ALS gene UNC13A. *Nature*. 603:124-130.

Mann, J.R., A.M. Gleixner, J.C. Mauna, E. Gomes, M.R. DeChellis-Marks, P.G. Needham, K.E. Copley, B. Hurtle, B. Portz, N.J. Pyles, L. Guo, C.B. Calder, Z.P. Wills, U.B. Pandey, J.K. Kofler, J.L. Brodsky, A. Thathiah, J. Shorter, and C.J. Donnelly. 2019. RNA Binding Antagonizes Neurotoxic Phase Transitions of TDP-43. *Neuron*. 102:321-338 e328.

Maurel, C., N.M. Scherer, L. Luu, R.A. Radford, A. Hogan, J. Merjane, A. Vidal-Itriago, E.K. Don, T. Chapman, S. Cull, P. Vourc'h, L. Lisowski, A. Lee, R.S. Chung, and M. Morsch. 2025. Critical impact of lysine 136 in TDP-43 phase separation, compartmentalization, and aggregation in living vertebrates. *iScience*. 28:112761.

Mehta, P.R., A.L. Brown, M.E. Ward, and P. Fratta. 2023. The era of cryptic exons: implications for ALS-FTD. *Mol Neurodegener*. 18:16.

Mo, M.H., J.L. Xie, Z.W. Chen, Q.Y. Yang, X.W. Hu, X.H. Zhou, J.L. Pathak, L.J. Wang, C. Liu, and L.J. Chen. 2024. Niobium Nanoparticles Activates Endothelial Tip Cells and Promotes Angiogenesis by FOXA1-PAK4-YAP Signaling Pathway. *Acs Appl Nano Mater*. 7:20123-20137.

Neumann, M., D.M. Sampathu, L.K. Kwong, A.C. Truax, M.C. Micsenyi, T.T. Chou, J. Bruce, T. Schuck, M. Grossman, C.M. Clark, L.F. McCluskey, B.L. Miller, E. Masliah, I.R. Mackenzie, H. Feldman, W. Feiden, H.A. Kretzschmar, J.Q. Trojanowski, and V.M. Lee. 2006. Ubiquitinated TDP-43 in frontotemporal lobar degeneration and amyotrophic lateral sclerosis. *Science*. 314:130-133.

Nguyen, H.N. 2022. Generation of iPSC-Derived Brain Organoids for Drug Testing and Toxicological Evaluation. *Methods Mol Biol*. 2474:93-105.

Pinarbasi, E.S., T. Cagatay, H.Y.J. Fung, Y.C. Li, Y.M. Chook, and P.J. Thomas. 2018. Active nuclear import and passive nuclear export are the primary determinants of TDP-43 localization. *Sci Rep*. 8:7083.

Putri, G.H., S. Anders, P.T. Pyl, J.E. Pimanda, and F. Zanini. 2022. Analysing high-throughput sequencing data in Python with HTSeq 2.0. *Bioinformatics*. 38:2943-2945.

Rubien, J., E. Lavorando, G. Padilla, and J. Shorter. 2022. Identifying Therapeutic Inhibitors of TDP43 Phase-Separation. *Faseb Journal*. 36.

Rummens, J., and S. Da Cruz. 2025. RNA-binding proteins in ALS and FTD: from pathogenic mechanisms to therapeutic insights. *Mol Neurodegener*. 20:64.

Seddighi, S., Y.A. Qi, A.L. Brown, O.G. Wilkins, C. Bereda, C. Belair, Y.J. Zhang, M. Prudencio, M.J. Keuss, A. Khandeshi, S. Pickles, S.E. Kargbo-Hill, J. Hawrot, D.M. Ramos, H. Yuan, J. Roberts, E.K. Sacramento, S.I. Shah, M.A. Nalls, J.M. Colon-Mercado, J.F. Reyes, V.H. Ryan, M.P. Nelson, C.N. Cook, Z. Li, L. Screven, J.Y. Kwan, P.R. Mehta, M. Zanovello, M. Hallegger, A. Shantaraman, L. Ping, Y. Koike, B. Oskarsson, N.P. Staff, D.M. Duong, A. Ahmed, M. Secrier, J. Ule, S. Jacobson, D.S. Reich, J.D. Rohrer, A. Malaspina, D.W. Dickson, J.D. Glass, A. Ori, N.T. Seyfried, M. Maragkakis, L. Petrucelli, P. Fratta, and M.E. Ward. 2024. Mis-spliced transcripts generate de novo proteins in TDP-43-related ALS/FTD. *Sci Transl Med*. 16:eadg7162.

Shorter, J. 2019. Phase separation of RNA-binding proteins in physiology and disease: An introduction to the JBC Reviews thematic series. *J Biol Chem*. 294:7113-7114.

Suk, T.R., and M.W.C. Rousseaux. 2020. The role of TDP-43 mislocalization in amyotrophic lateral sclerosis. *Mol Neurodegener*. 15:45.

Tziortzouda, P., L. Van Den Bosch, and F. Hirth. 2021. Triad of TDP43 control in neurodegeneration: autoregulation, localization and aggregation. *Nat Rev Neurosci*. 22:197-208.

van Eersel, J., Y.D. Ke, A. Gladbach, M. Bi, J. Gotz, J.J. Kril, and L.M. Ittner. 2011. Cytoplasmic accumulation and aggregation of TDP-43 upon proteasome inhibition in cultured neurons. *PLoS One*. 6:e22850.

Yu, H., S. Lu, K. Gasior, D. Singh, S. Vazquez-Sanchez, O. Tapia, D. Toprani, M.S. Beccari, J.R. Yates, 3rd, S. Da Cruz, J.M. Newby, M. Lafarga, A.S. Gladfelter, E. Villa, and D.W. Cleveland. 2021. HSP70 chaperones RNA-free TDP-43 into anisotropic intranuclear liquid spherical shells. *Science*. 371.

Zeng, Y., A. Lovchykova, T. Akiyama, S.L. Rayner, V. Maheswari Jawahar, C. Liu, O. Sianto, C. Guo, A. Calliari, M. Prudencio, D.W. Dickson, L. Petrucelli, and A.D. Gitler. 2025. TDP-43 nuclear loss in FTD/ALS causes widespread alternative polyadenylation changes. *Nat Neurosci*. 28:2180-2189.

Zhang, J., J. Hu, R. Liu, T. Zhou, X. Luo, P. Liang, Z. Xie, Q. Zhao, Y. Chen, D. Du, C. Liu, Y. Zheng, D. Li, and B. Wang. 2025a. YAP maintains the dynamics of TDP-43 condensates and antagonizes TDP-43 pathological aggregates. *Nat Cell Biol*. 27:1148-1160.

Zhang, Q., M. Liu, X. Fan, N. Chin, Y. Xu, J. Suh, S. Amniouel, K. Linask, J. Zou, M. Hafner, L. Ma, W. Zheng, and Y. Ye. 2025b. A human forebrain organoid model phenocopies dysregulated RNA and protein homeostasis in ALS/FTD-associated TDP-43 proteinopathies. *BioRxiv*.

## Figure legends

**Figure 1 A chemical genetic screen identifies TDP-43 phase modulators**

**(A)** The workflow of the chemical genetic screen.

**(B)** Dose dependent reduction of anisosome number by identified chemicals. DLD1 TDP-43 2KQ-Clover cells were treated with doxycycline to induce anisosome for 24 h and then treated with the drugs as indicated for 15 h. Cells were imaged for anisosome count.

**Figure 2 Two distinct types of TDP-43 phase modulators**

**(A)** DLD1 TDP-43 2KQ-Clover cells treated with doxycycline for 24 h were further treated with the indicated compounds for 6 h and imaged (SPA, Spautin-1, 5 μM; KPT, KPT-276, 15 μM; CP, CP-673451, 30 μM; TRP, Tripterin, 1 μM; BTZ, Bortezomib, 10 nM). Scale bar, 5 μm.

**(B)** FRAP analyses of anisosomes after treatment with the indicated drugs for 3-5 h. Circles indicate bleached areas. Scale bars, 1 μm.

**(C, D)** Quantification of the experiments represented in B. FL, Fluorescence.

**(E)** Reverse FRAP analyses of anisosome dynamics. The areas indicated by the dashed lines were bleached. Scale bar, 5 μm.

**(F)** Quantification of the fluorescence loss over time in unbleached anisosomes as shown in E. N=4-6.

**(G)** Quantification of the initial rate of fluorescence loss in unbleached anisosomes. ****, $p<0.0001$; ***, $p<0.001$ by unpaired Student's t-test.

**Figure 3 A genome-wide siRNA screen identifies modifiers of TDP43 phase behavior**

**(A)** The workflow of the siRNA genetic screen. GW, genome-wide; AS, anisosome; HT, high-throughput.

**(B)** Pathway analysis of genes whose knockdown reduces anisosome number in cells. The relative anisosome count are indicated by both color and size of the nodes.

**(C)** GO molecular function analysis of TDP-43 phase modifiers.

**(D)** A list of identified genes linked to ALS in C.

**Figure 4 Anisosome phase behavior is modulated by RNA splicing and protein translation**

**(A)** The splicing inhibitor Pladienolide-B (PlaB) reduces anisosome number in a dose dependent manner. Representative images of anisosome-induced cells treated with DMSO (control), 5 nM, or 20 nM PlaB for 16 h. Scale bar: 10 μm.

**(B)** Quantification showing the number of anisosome (AS) per cell in TDP-43 2KQ-Clover cells treated with PlaB as indicated. * $p<0.05$, ** $p<0.01$, **** $p<0.0001$ by One-way ANOVA. n=3 biological repeats.

**(C)** Representative FRAP images of anisosomes in cells treated for 16 h with DMSO or PlaB (20 nM). BB, before photobleaching, right after photobleaching (0 s), or 4 and 30 seconds after photobleaching (4 s and 30 s). Scale bar, 1 µm.

**(D)** The graph shows the quantification of the remaining TDP-43 fluorescence (FL) in C. Error bars indicate mean ± SD, N = 28 for control and 23 for PlaB-treated cells.

**(E)** Live cell imaging of anisosome fusion in TDP-43 2KQ-Clover cells treated with 20 nM PlaB for 5 h before tracking the fusion. Representative images from Movie S1 showing fusion events indicated by arrows. Scale bar, 1 µm.

**(F)** Representative images of anisosome-induced (24 h) cells treated with DMSO (control) or ANS (200 nM) for 16 h. Scale bar, 1 µm.

**(G)** Quantification of the number of anisosomes per cell in randomly selected images of DMSO-, Cycloheximide (CHX)-, or ANS-treated cells. **** $p < 0.0001$ by one-way ANOVA; each dot represents an image with at least 20 cells counted. n=3 biological repeats.

**(H)** Quantification of anisosome size in control or cells treated with CHX or ANS. ****, $p < 0.0001$ by One-way ANOVA. n=3 biological repeats. AU, arbitrary unit.

**(I)** As in **C** except that anisosome-induced cells were treated with CHX or ANS before photobleaching. Scale bar 1 µm.

**(J)** Quantification of fluorescence recovery in CHX- or ANS-treated cells vs the DMSO control.

**Figure 5 XPO1 regulates anisosome liquid-to-solid transition**

**(A)** Pharmacological inhibition of XPO-1 with Leptomycin B (LMB) reduces the number of anisosome. The graph on top indicates the experimental design. Arrows show cells with enlarged anisosomes. Scale bar 10 µm

**(B)** Quantification of anisosome numbers per cell in experiments represented by A. Error bars indicate mean ± SD; **** $p <0.0001$ by one-way ANOVA. n=3 biological repeats.

**(C)** LMB dose dependently reduces anisosome number. Anisosome were induced in TDP-43 2KQ-Clover cells followed by treatment with LMB at the indicated concentrations for 16 h. The histogram shows the distribution of cells (50-90 cells/condition) by anisosome count.

**(D)** FRAP experiments demonstrate that anisosomes remain in a liquid phase following LMB treatment (200 nM, 16 h). Anisosome-induced (24 h) cells were treated with DMSO or LMB for 16 h and then photobleached at the indicated areas. Scale bar 1 µm.

**(E)** Quantification of the FRAP experiment in D.

**(F)** Time-lapse confocal microscopy detects anisosome fusion after LMB (200 nM, 5 h) treatment in TDP-43 2KQ-Clover cells. Arrows indicate fusion events. Scale bar, 1 µm

**(G)** Overexpression of mCherry-tagged XPO-1 in TDP-43 2KQ-Clover cells induces cytoplasmic TDP-43 puncta. TDP-43 2KQ-Clover cells (green) transfected with mCherry-XPO1 (red) were stained with DAPI (blue) to label nuclei (dashed lines). Cells were imaged 48 h post-transfection. Panels 1, 2 show a representative confocal section, while panels 3-6 show reconstructed 3-D views. The position and volume of anisosomes were also presented in magenta in a surface-rendered view (SRV) in panel 5. The arrow in panel 3 indicates an example of cytoplasmic TDP-43 aggregate. Scale bar, 10 µm.

**(H)** Quantification of the percentage of cells showing cytosolic TDP-43 puncta in XPO-1 positive (pos) and negative (neg) cells in randomly selected fields from 3 independent experiments. **** $p < 0.0001$ by unpaired Student's t-test.

**(I)** FRAP-based confocal imaging reveals the transition of anisosomes into a gel-like state upon XPO-1 overexpression. Scale bar, 1 µm.

**(J)** Anisosome formation changes endogenous XPO-1 localization. TDP-43 2KQ-Clover before or after anisosome induction were stained with anti-XPO-1 antibodies (red) and DAPI (blue). The bleached areas were indicated by dashed lines. Scale bar, 10 µm.

**(K)** Quantification of nuclear endogenous XPO-1 levels in individual cells (indicated by dots) before or after anisosome induction. **** $p < 0.001$ by unpaired Student's t-test. n=2 independent repeats.

**(L)** A schematic model depicting how the nuclear XPO-1 activity influences TDP-43 liquid-to-phase transition. AS, anisosome.

**Figure 6 Inhibition of XPO-1 reduces TDP-43 hyperphosphorylation but only partially restore neuronal gene expression in K181E organoids**

**(A)** Confocal fluorescence imaging reveals significant reduction in phosphorylated TDP-43 (p-TDP43) in K181E/K181E organoids following KPT-276 treatment. Organoids of the indicated genotypes at day 87 were treated with DMSO as a control, or with KPT-276 (20 nM) for 35 days. Organoids were fixed, sectioned, and stained with antibodies against TUJ1, a neuronal marker (Magenta), TDP-43 (green) and p-TDP-43 (red). n= 3-5 organoids from two individual batches.

**(B)** Quantification of p-TDP-43 Mean Spot Volume (top) and percentage of cells lacking nuclear TDP-43 (bottom) in experiments represented by **A**. Error bars indicate mean ± s.e.m., * $p < 0.05$, **** $p < 0.0001$ by one-way ANOVA, n=3 organoids.

**(C)** Gene Ontology (GO) analysis of genes whose expression was disrupted in K181E/K181E organoids but restored by KPT-267 as shown in Supplemental Fig. S3. BP, Biological Pathway; CC, Cellular Component; MF, Molecular Function.

Figure 1

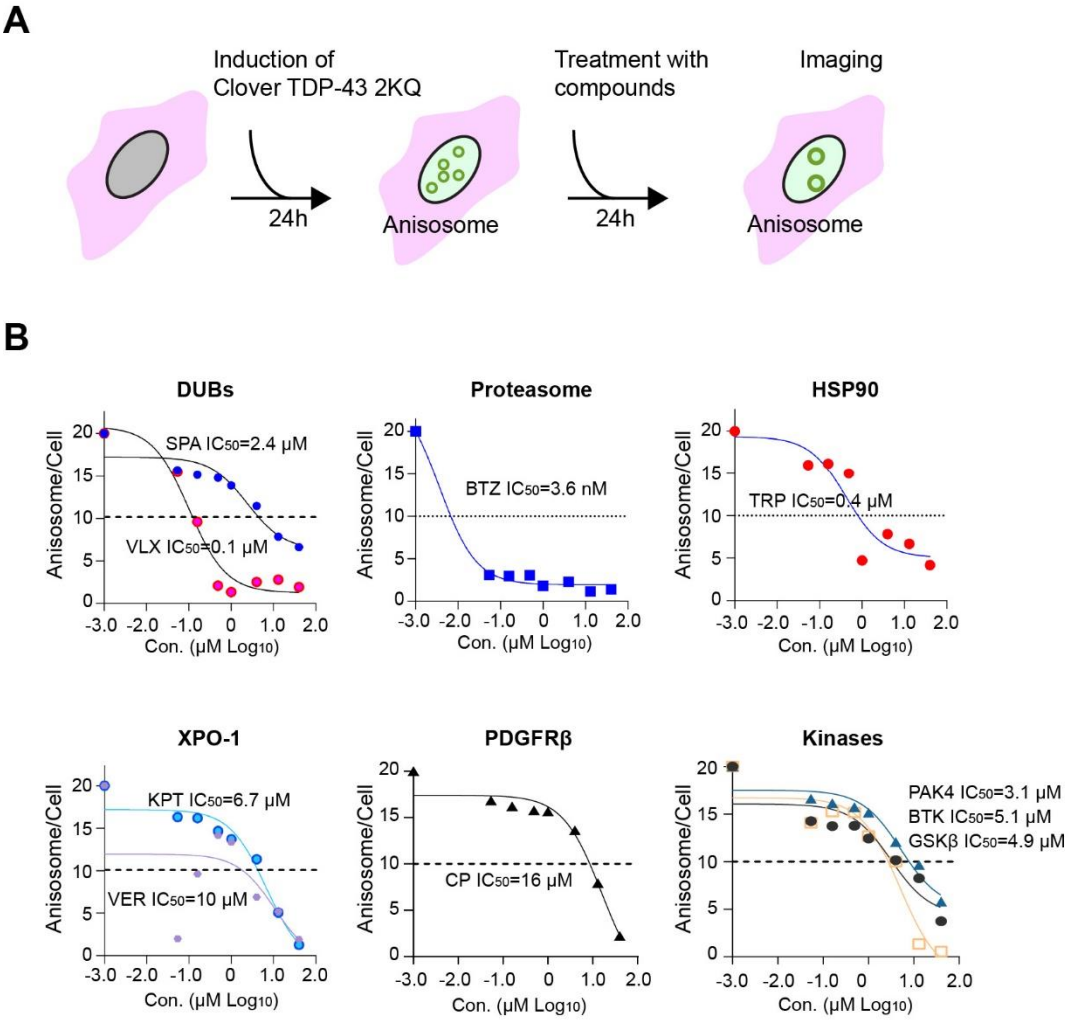
A
Induction of
Clover TDP-43 2KQ
24h
Anisosome
Treatment with
compounds
24h
Imaging
Anisosome
B
DUBs
SPA IC50=2.4 μM
VLX IC50=0.1 μM
Proteasome
BTZ IC50=3.6 nM
HSP90
TRP IC50=0.4 μM
XPO-1
KPT IC50=6.7 μM
VER IC50=10 μM
PDGFRβ
CP IC50=16 μM
Kinases
PAK4 IC50=3.1 μM
BTK IC50=5.1 μM
GSKβ IC50=4.9 μM
Anisosome/Cell
Con. (μM Log10)

Figure 2

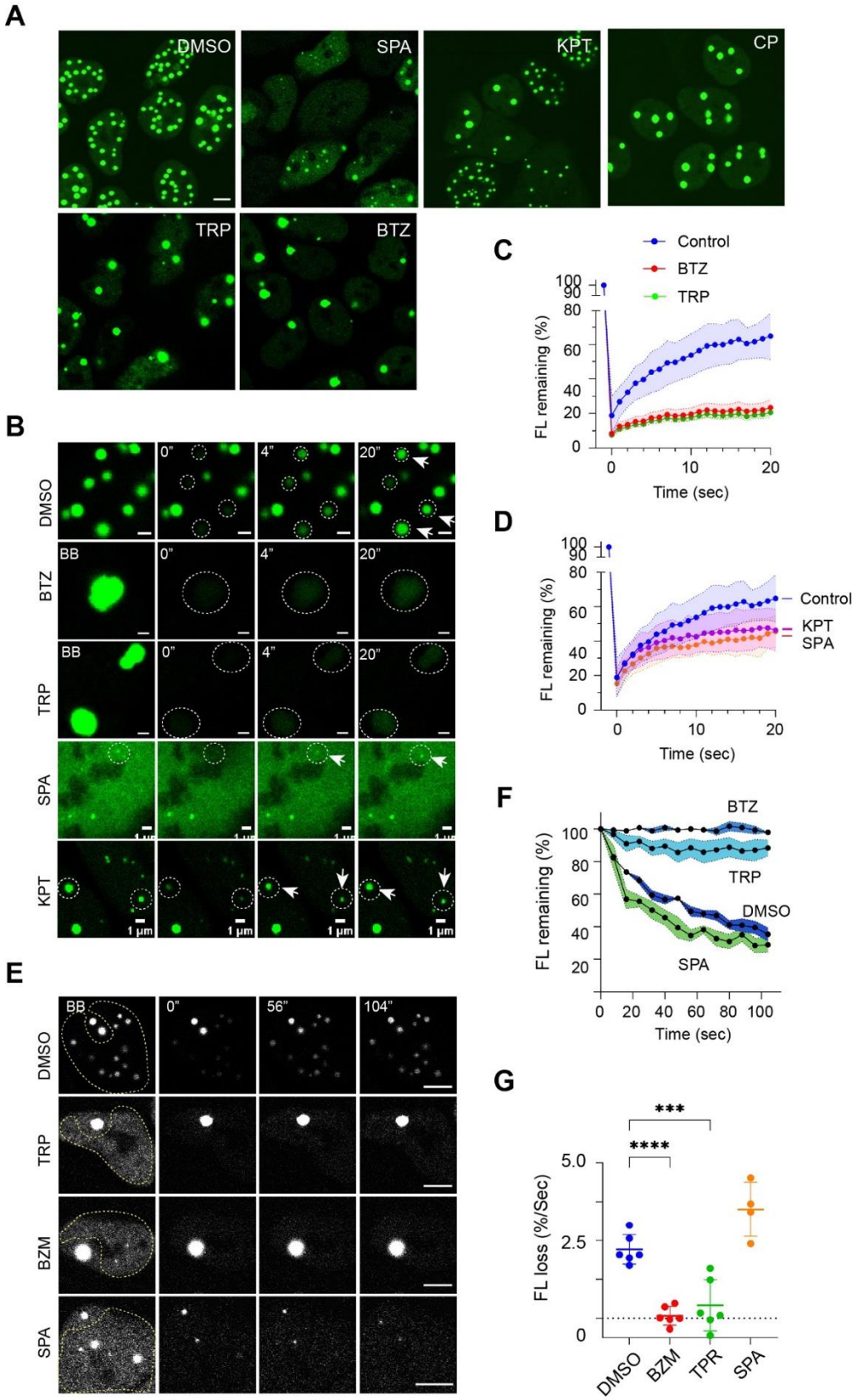


739

740

Figure 3

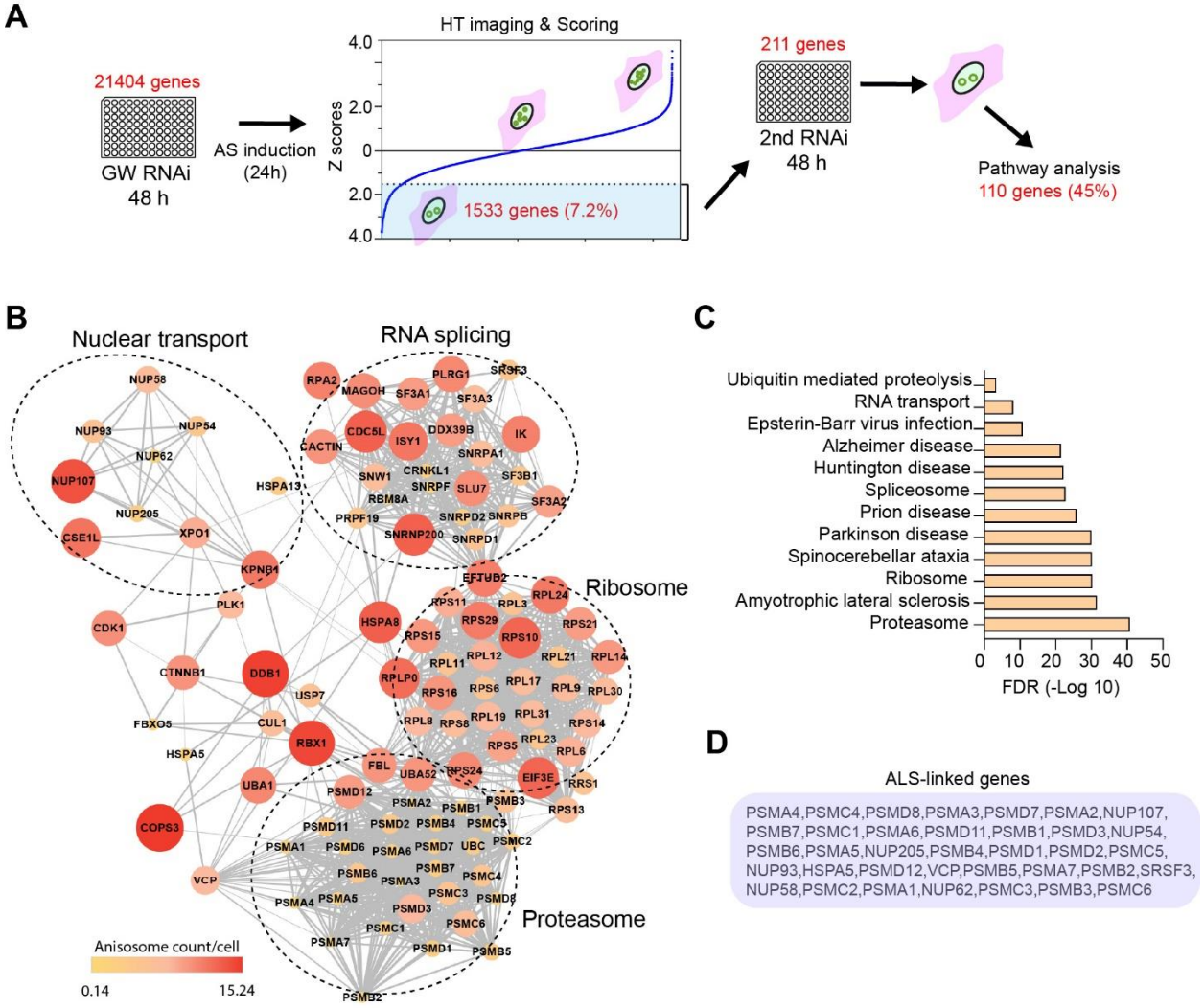
A
21404 genes
GW RNAi
48 h
AS induction
(24h)
HT imaging & Scoring
Z scores
4.0
2.0
0
2.0
4.0
1533 genes (7.2%)
211 genes
2nd RNAi
48 h
Pathway analysis
110 genes (45%)
B
Nuclear transport
RNA splicing
Ribosome
Proteasome
Anisosome count/cell
0.14
15.24
C
Ubiquitin mediated proteolysis
RNA transport
Epsterin-Barr virus infection
Alzheimer disease
Huntington disease
Spliceosome
Prion disease
Parkinson disease
Spinocerebellar ataxia
Ribosome
Amyotrophic lateral sclerosis
Proteasome
0 10 20 30 40 50
FDR (-Log 10)
D
ALS-linked genes
PSMA4,PSMC4,PSMD8,PSMA3,PSMD7,PSMA2,NUP107,
PSMB7,PSMC1,PSMA6,PSMD11,PSMB1,PSMD3,NUP54,
PSMB6,PSMA5,NUP205,PSMB4,PSMD1,PSMD2,PSMC5,
NUP93,HSPA5,PSMD12,VCP,PSMB5,PSMA7,PSMB2,SRSF3,
NUP58,PSMC2,PSMA1,NUP62,PSMC3,PSMB3,PSMC6

Figure 4

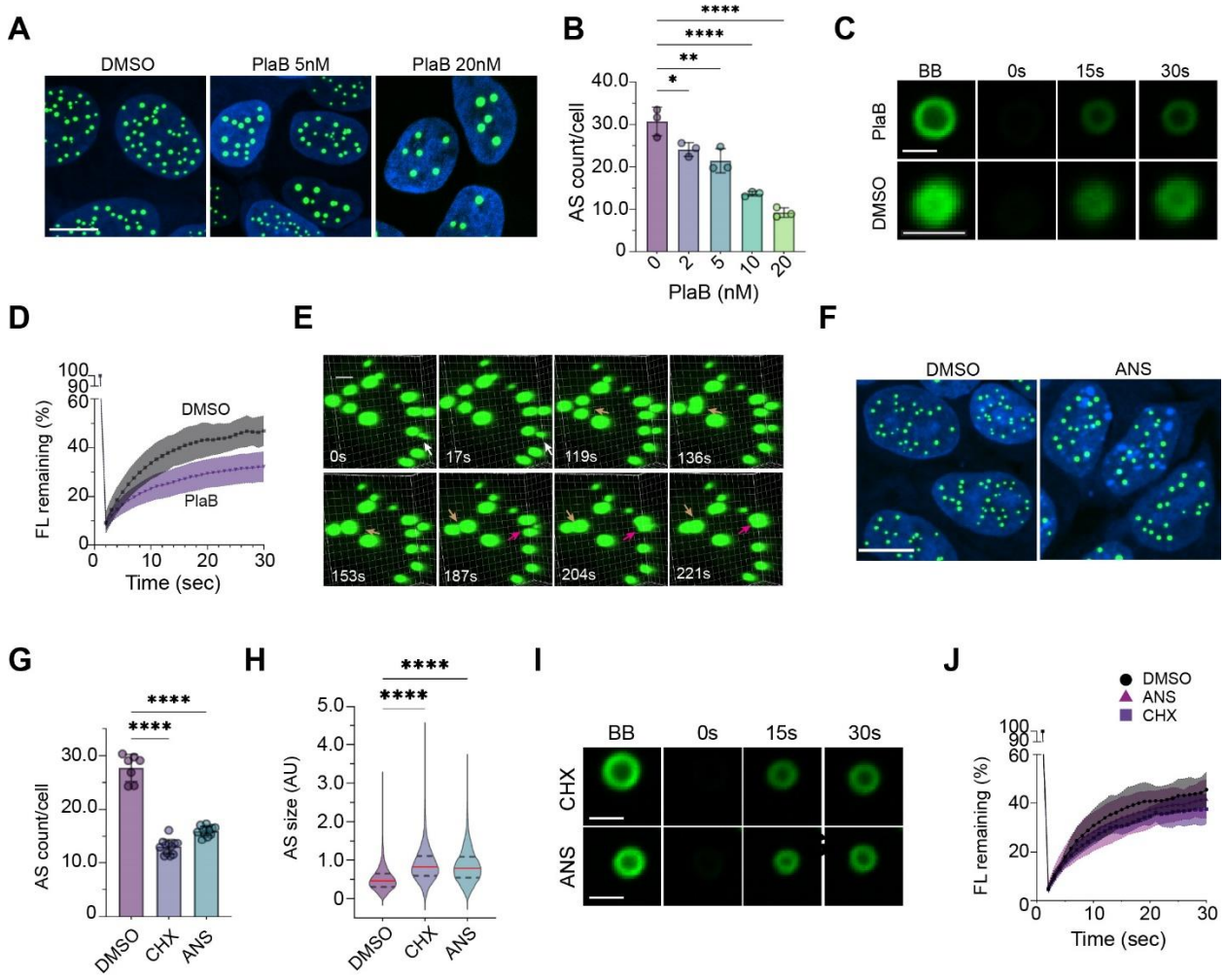
A
DMSO
PlaB 5nM
PlaB 20nM
B
AS count/cell
PlaB (nM)
C
BB
0s
15s
30s
PlaB
DMSO
D
FL remaining (%)
Time (sec)
DMSO
PlaB
E
0s
17s
119s
136s
153s
187s
204s
221s
F
DMSO
ANS
G
AS count/cell
DMSO
CHX
ANS
H
AS size (AU)
DMSO
CHX
ANS
I
BB
0s
15s
30s
CHX
ANS
J
DMSO
ANS
CHX
FL remaining (%)
Time (sec)

Figure 5

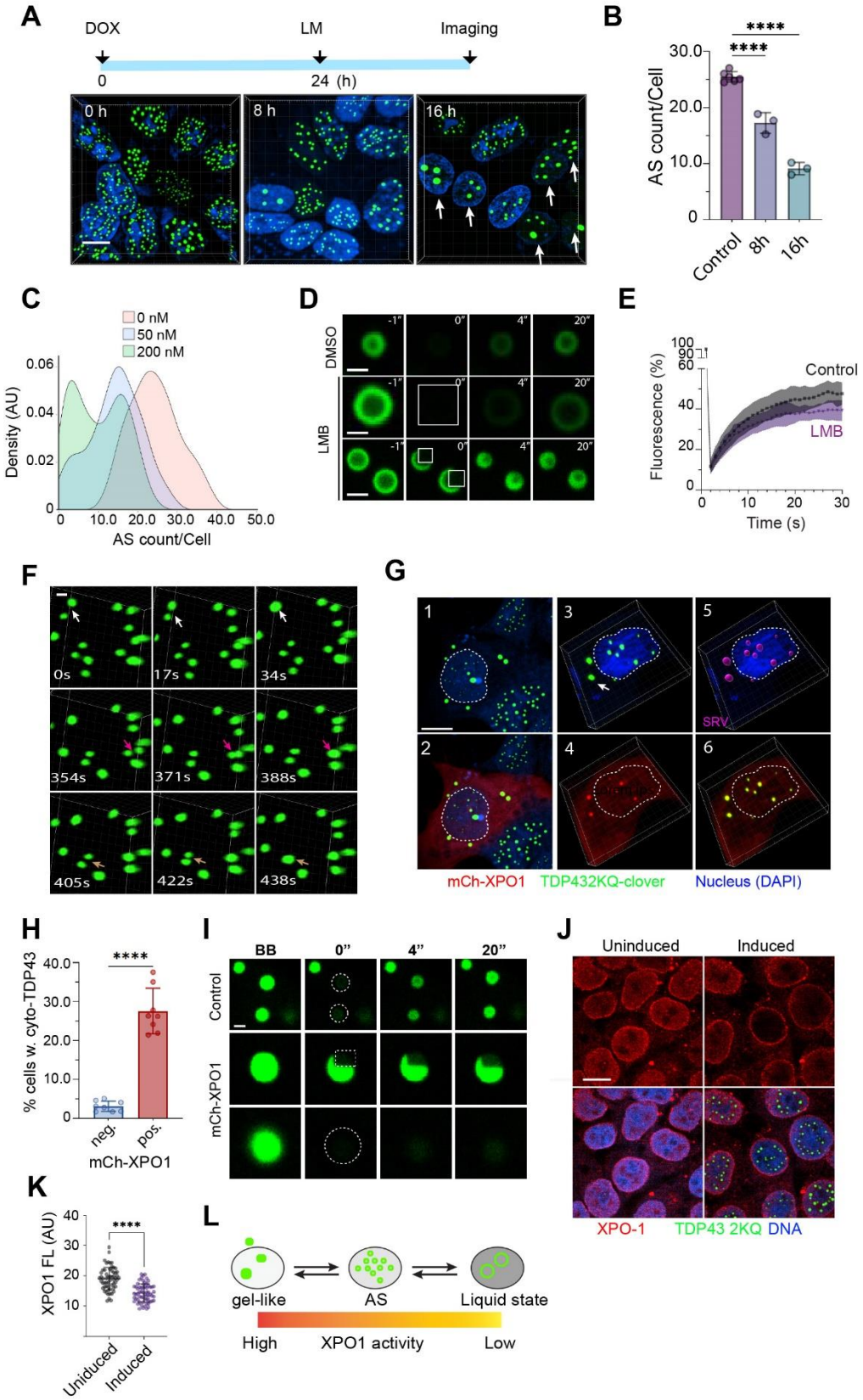
A
DOX
LM
Imaging
0
24 (h)
0 h
8 h
16 h
B
****
****
AS count/Cell
30.0
20.0
10.0
0
Control
8h
16h
C
0 nM
50 nM
200 nM
Density (AU)
0.06
0.04
0.02
0
0
10.0
20.0
30.0
40.0
50.0
AS count/Cell
D
DMSO
LMB
-1"
0"
4"
20"
E
Fluorescence (%)
100
90
60
40
20
0
Control
LMB
0
10
20
30
Time (s)
F
0s
17s
34s
354s
371s
388s
405s
422s
438s
G
1
2
3
4
5
6
SRV
mCh-XPO1
TDP432KQ-clover
Nucleus (DAPI)
H
****
% cells w. cyto-TDP43
40.0
30.0
20.0
10.0
0
neg.
pos.
mCh-XPO1
I
BB
0"
4"
20"
Control
mCh-XPO1
J
Uninduced
Induced
XPO-1
TDP43 2KQ
DNA
K
****
XPO1 FL (AU)
40
30
20
10
Uniduced
Induced
L
gel-like
AS
Liquid state
High
XPO1 activity
Low

745

Figure 6

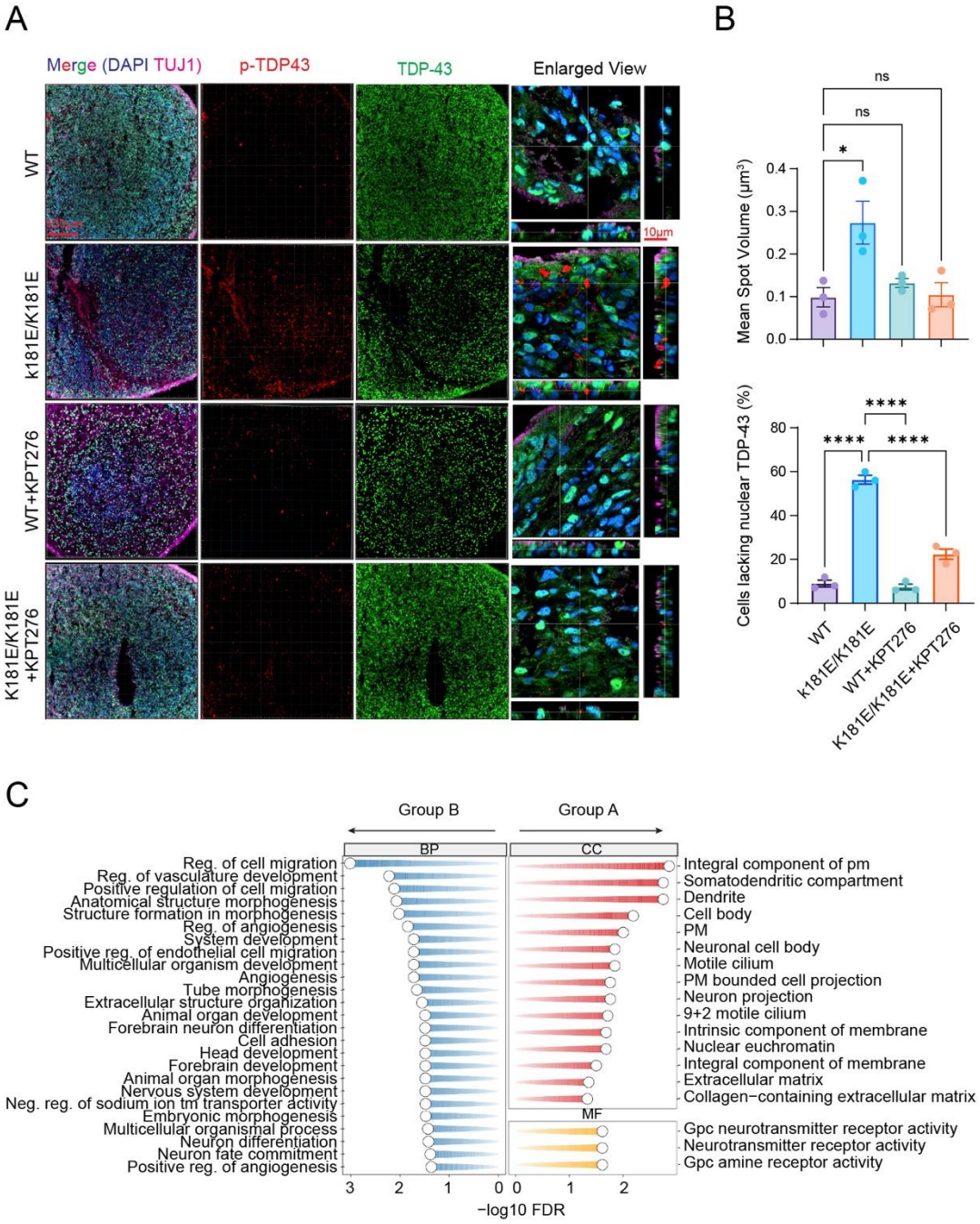
A
Merge (DAPI TUJ1)
p-TDP43
TDP-43
Enlarged View
WT
k181E/K181E
WT+KPT276
K181E/K181E +KPT276
10μm
B
Mean Spot Volume (μm³)
ns
ns
*
Cells lacking nuclear TDP-43 (%)
****
****
****
WT
k181E/K181E
WT+KPT276
K181E/K181E+KPT276
C
Group B
Group A
BP
CC
MF
Reg. of cell migration
Reg. of vasculature development
Positive regulation of cell migration
Anatomical structure morphogenesis
Structure formation in morphogenesis
Reg. of angiogenesis
System development
Positive reg. of endothelial cell migration
Multicellular organism development
Angiogenesis
Tube morphogenesis
Extracellular structure organization
Animal organ development
Forebrain neuron differentiation
Cell adhesion
Head development
Forebrain development
Animal organ morphogenesis
Nervous system development
Neg. reg. of sodium ion tm transporter activity
Embryonic morphogenesis
Multicellular organismal process
Neuron differentiation
Neuron fate commitment
Positive reg. of angiogenesis
Integral component of pm
Somatodendritic compartment
Dendrite
Cell body
PM
Neuronal cell body
Motile cilium
PM bounded cell projection
Neuron projection
9+2 motile cilium
Intrinsic component of membrane
Nuclear euchromatin
Integral component of membrane
Extracellular matrix
Collagen−containing extracellular matrix
Gpc neurotransmitter receptor activity
Neurotransmitter receptor activity
Gpc amine receptor activity
−log10 FDR

**Supplemental Materials**

Movie S1 PlaB treatment induces anisosome fusion.

Movie S2 Blocking XPO-1-mediated nuclear export induces anisosome fusion.

**Supplemental Tables**

Table S1 A chemical genetic screen identified compounds that reduce anisosome numbers.

Table S2 A genome-wide siRNA screen identified potential anisosome regulators.

Table S3 Top 110 genes confirmed from a secondary screen as modulators of anisosome dynamics.

Table S4 Differentially expressed genes in K181E organoids rescued by KPT-276 (KPT).

**Supplemental Figures**

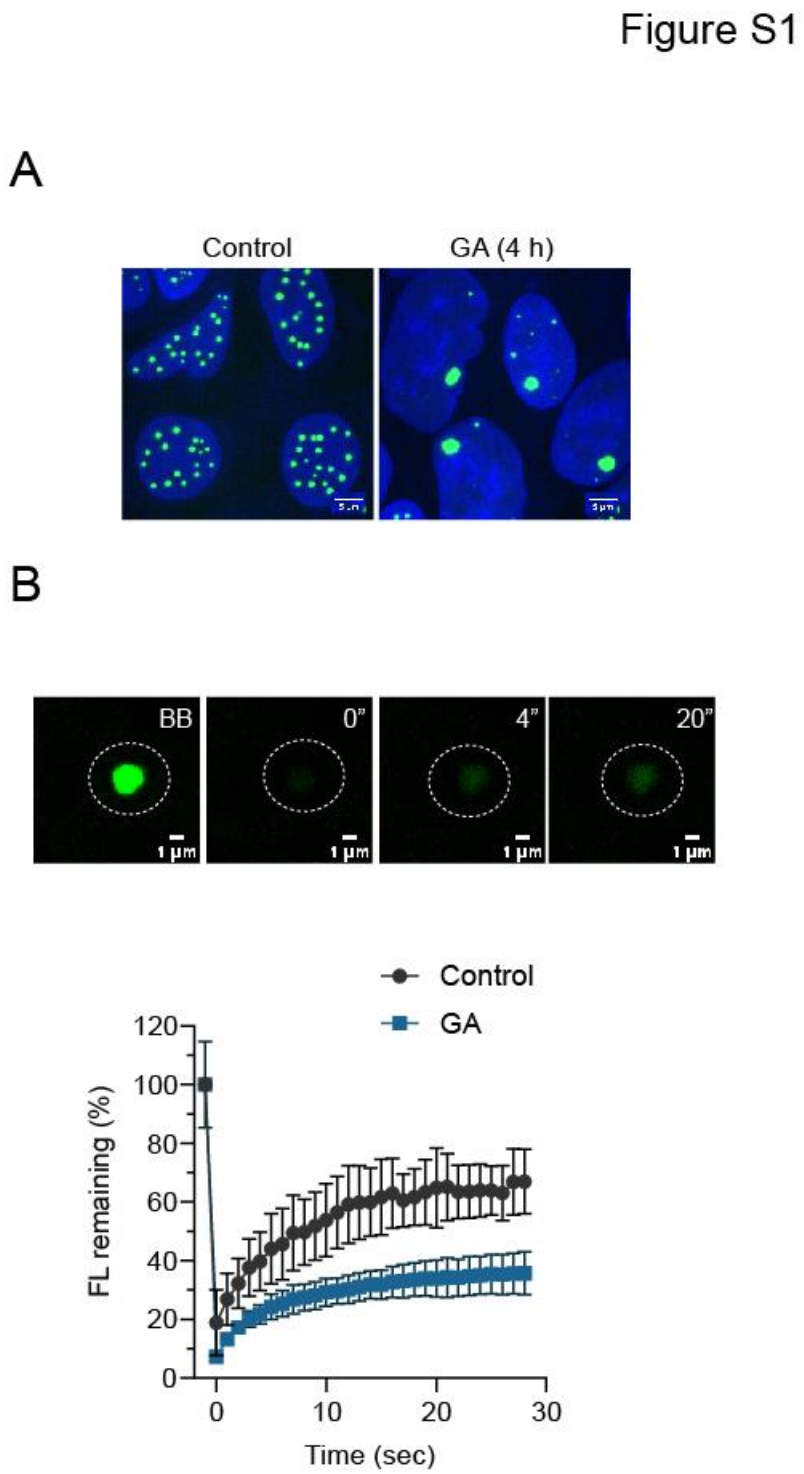


**Figure S1. HSP90 inhibitor Geldanamycin converts TDP-43 anisosome to a gel-like state**

**(A)** DLD1 cells were treated with doxycycline to induce anisosome formation and then treated with Geldanamycin (GA) at 10 μM for 4 h. Cells were stained with Hoechst (Blue) and imaged by a confocal microscope. Scale bar, 5 μm.

**(B)** A TDP-43-bearing anisosome (dashed circle) in a GA-treated cell was photobleached and then imaged. Scale bar, 1 μm. The graph shows the quantification. Error bars, s.e.m. (N>5 anisosomes). FL, fluorescence.

Figure S2

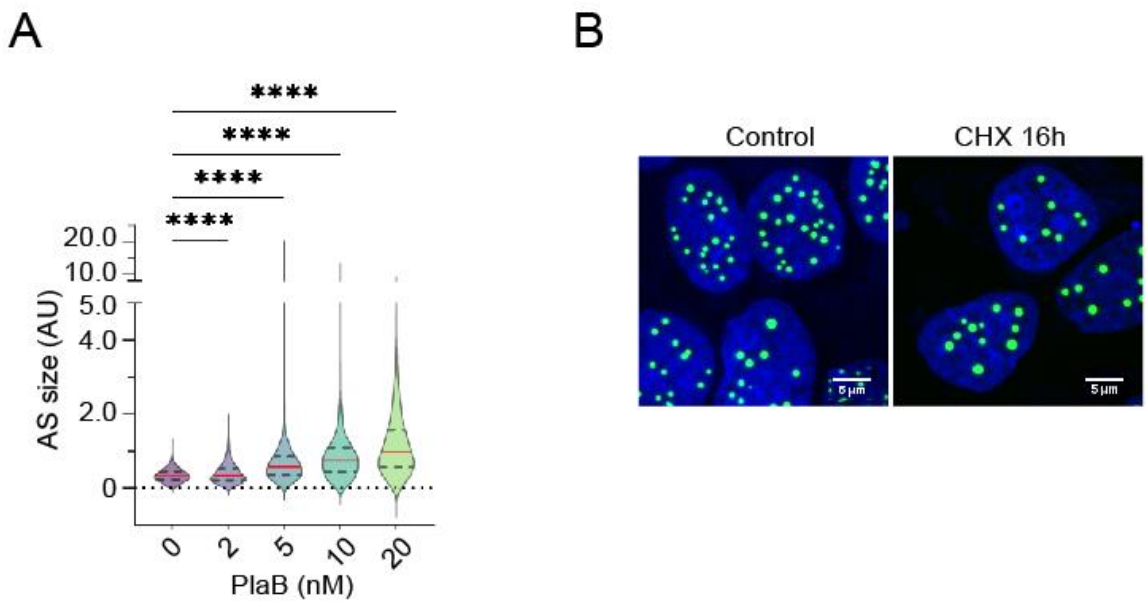


**Figure S2. The impact of splicing inhibitor and translation inhibitor on anisosomes**

**(A)** A violin plot showing the relative size distribution of anisosomes (AS) in DLD1 cells treated with Pladienolide-B at the indicated concentration for 16 h. ****, $p<0.0001$ by one-way ANOVA. n=3 biological repeats.

**(B)** DLD1 cells were treated with doxycycline to induce anisosome formation and then treated with Cycloheximide (CHX) at 20 μg/mL or DMSO as a control for 16 h. Cells were stained with Hoechst (Blue) and imaged by a confocal microscope. Scale bar, 5 μm.

Figure S3

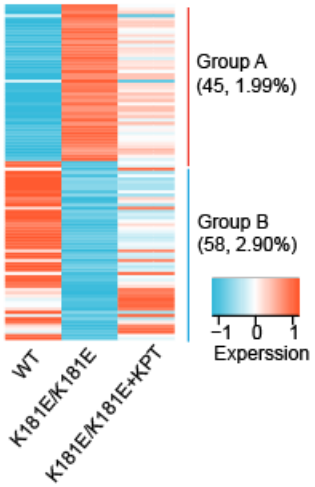


**Figure S3. KPT-276 modestly reverses gene expression defects in K181E mutant organoids**

Heatmap showing genes whose expression was altered in K181E/K181E organoids and restored after KPT-276 treatment.